

Guanidinium-Assisted Surface Matrix Engineering for Highly Efficient Perovskite Quantum Dot Photovoltaics

Xufeng Ling, Jianyu Yuan,* Xuliang Zhang, Yuli Qian, Shaik M. Zakeeruddin, Bryon W. Larson, Qian Zhao, Junwei Shi, Jiacheng Yang, Kang Ji, Yannan Zhang, Yongjie Wang, Chunyang Zhang, Steffen Duhm,* Joseph M. Luther, Michael Grätzel,* and Wanli Ma*

Metal halide perovskite quantum dots (Pe-QDs) are of great interest in new-generation photovoltaics (PVs). However, it remains challenging in the construction of conductive and intact Pe-QD films to maximize their functionality. Herein, a ligand-assisted surface matrix strategy to engineer the surface and packing states of Pe-QD solids is demonstrated by a mild thermal annealing treatment after ligand exchange processing (referred to as “LE-TA”) triggered by guanidinium thiocyanate. The “LE-TA” method induces the formation of surface matrix on CsPbI_3 QDs, which is dominated by the cationic guanidinium (GA^+) rather than the SCN^- , maintaining the intact cubic structure and facilitating interparticle electrical interaction of QD solids. Consequently, the GA -matrix-confined CsPbI_3 QDs exhibit remarkably enhanced charge mobility and carrier diffusion length compared to control ones, leading to a champion power conversion efficiency of 15.21% when assembled in PVs, which is one of the highest among all Pe-QD solar cells. Additionally, the “LE-TA” method shows similar effects when applied to other Pe-QD PV systems like CsPbBr_3 and FAPbI_3 (FA = formamidinium), indicating its versatility in regulating the surfaces of various Pe-QDs. This work may afford new guidelines to construct electrically conductive and structurally intact Pe-QD solids for efficient optoelectronic devices.

The remarkable tunability in size and composition has endowed semiconducting colloidal quantum dots (CQDs) with numerous superiorities over conventional bulk materials due to their unique quantum confinement effect.^[1,2] Quite recently, nanometer-sized lead halide perovskites (APbX_3 , $\text{A} = \text{Cs}$ or formamidinium (FA) and $\text{X} = \text{Cl}$, Br , I , or mixed) QDs or, more broadly, nanocrystals have been successfully synthesized, offering excellent tunability of absorption and emission across the full visible spectrum.^[3,4] The perovskite QDs (Pe-QDs) exhibit combinative advantages of conventional metal chalcogenides CQDs and emerging metal halide perovskites, such as high photoluminescence quantum yields (PLQYs), flexible compositional control, and high defect tolerance.^[5,6] In addition, their colloidal synthesis creates a Pe-QDs ink that decouples crystal growth from film formation, enabling construction of crystalline films,^[7,8] and more impressively, perovskite heterostructures

X. Ling, Prof. J. Yuan, X. Zhang, Y. Qian, J. Shi, J. Yang,
 K. Ji, Y. Zhang, Y. Wang, Prof. S. Duhm, Prof. W. Ma
 Institute of Functional Nano & Soft Materials (FUNSOM)
 Jiangsu Key Laboratory for Carbon-Based Functional Materials and Devices
 Joint International Research Laboratory of Carbon-Based
 Functional Materials and Devices
 Soochow University
 199 Ren-Ai Road, Suzhou Industrial Park
 Suzhou, Jiangsu 215123, P. R. China
 E-mail: jyyuan@suda.edu.cn; duhm@suda.edu.cn; wlma@suda.edu.cn
 Dr. S. M. Zakeeruddin, C. Zhang, Prof. M. Grätzel
 Laboratory of Photonics and Interfaces (LPI)
 Institute of Chemical Sciences and Engineering
 École Polytechnique Fédérale de Lausanne (EPFL), Station 6, Lausanne
 CH-1015, Switzerland
 E-mail: michael.graetzel@epfl.ch
 Dr. B. W. Larson, Q. Zhao, Prof. J. M. Luther
 Chemistry & Nanoscience Center
 National Renewable Energy Laboratory
 Golden, CO 80401, USA

 The ORCID identification number(s) for the author(s) of this article can be found under <https://doi.org/10.1002/adma.202001906>.

DOI: 10.1002/adma.202001906

with diverse constituents through a facile layer-by-layer process.^[9,10] Moreover, tunable surface chemistry of QDs allows for various processing conditions, which enables Pe-QDs to be compatible with many other PV materials and versatile device architectures. Among the Pe-QDs family, $\alpha\text{-CsPbI}_3$ with cubic symmetry (bandgap, $E_g = 1.73$ eV) is the most popular light absorber for PV application.^[11] Swarnkar et al. pioneered the low-temperature processed, stable and over 10% efficiency CsPbI_3 QD solar cells (QDSCs) by leveraging the surface energy of QDs.^[7] Although we achieved an extremely high open-circuit voltage (V_{OC}) of ≈ 1.3 V^[12] and further increased power conversion efficiency (PCE) over 14% for CsPbI_3 based QDSCs,^[13] the optimized performance (PCE = 14.32%)^[14] is still significantly lower than that of all-inorganic perovskite thin-film solar cells.^[15] And most CsPbI_3 QD devices suffer from low short-circuit current density (J_{SC}).

The well-established strategies involved in conventional lead chalcogenides colloidal QDs^[16] are not compatible with the CsPbI_3 QDs owing to their intrinsic ionic and susceptible features,^[3,5] making it challenging to fabricate structurally intact

CsPbI_3 QD solids. Moreover, the ligands stabilizing Pe-QDs consist of long hydrocarbon chains, acting as a direct tunneling barrier for charge transport when assembled into arrays, which impedes the construction of electrically conductive QD films.^[3,4] Here, we report ligand-assisted surface matrix engineering by a thermal annealing treatment after ligand exchange processing (referred to as “LE-TA”) to rationally tune Pe-QD surfaces. Specifically, large-size organic cation (compared to Cs^+), guanidinium (GA^+), was coated onto CsPbI_3 QD surfaces through ligand exchange followed by a mild thermal annealing process ($<100^\circ\text{C}$, referred to as “TA”). The GA-assisted surface matrix engineering improved the electrical coupling and carrier transport between QDs. Consequently, a champion PCE of 15.21% together with a high J_{SC} approaching 16 mA cm^{-2} were obtained, situating our system at the forefront of all reported CsPbI_3 QDSCs.^[8–10,12–14,17–20]

The CsPbI_3 Pe-QDs stabilized by oleate (OA^-) and oleylammonium (OAm^+) ligands were synthesized using a reported hot-injection method^[9] yielding an average size of $\approx 9 \text{ nm}$ (Figure S1, Supporting Information) and deposited through a layer-by-layer spin-coating from their octane solution. Each layer of the QD films was washed by methyl acetate (MeOAc)

that partially removed the long native ligands and enabled the deposition of subsequent layers. The GA-matrix-capped QD solids were achieved by dipping the stacked QD films into a guanidinium thiocyanate (GASCN, chemical structures of GASCN and OAm^+ are shown in Figure S2, Supporting Information) solution in ethyl acetate (EtOAc), followed by a mild thermal annealing process. Full details of the film deposition are given in the Experimental Section. We depict the potential GA-matrix formation process and its effects on charge transport in CsPbI_3 QDs. As shown in Figure 1a, the as-synthesized CsPbI_3 QDs with long ligands are electrically isolating, impeding charge transport. The removal of these long insulating ligands is crucial for constructing conductive QD solids, which, however, induces the formation of surface defects due to the loss of binding motifs.^[7] These charge trapping defects also increase non-radiative recombination losses in QDs (Figure 1b), and deteriorate the PV performance.^[16] Here, the thin GA-matrix formed through “LE-TA” procedure shields the surface defect sites from trapping charges (right bottom in Figure 1a), and induces enhanced electrical coupling between neighboring QDs due to closer packing (Figure 1b). As we show, the well-maintained integrity of the nanocrystalline structure and

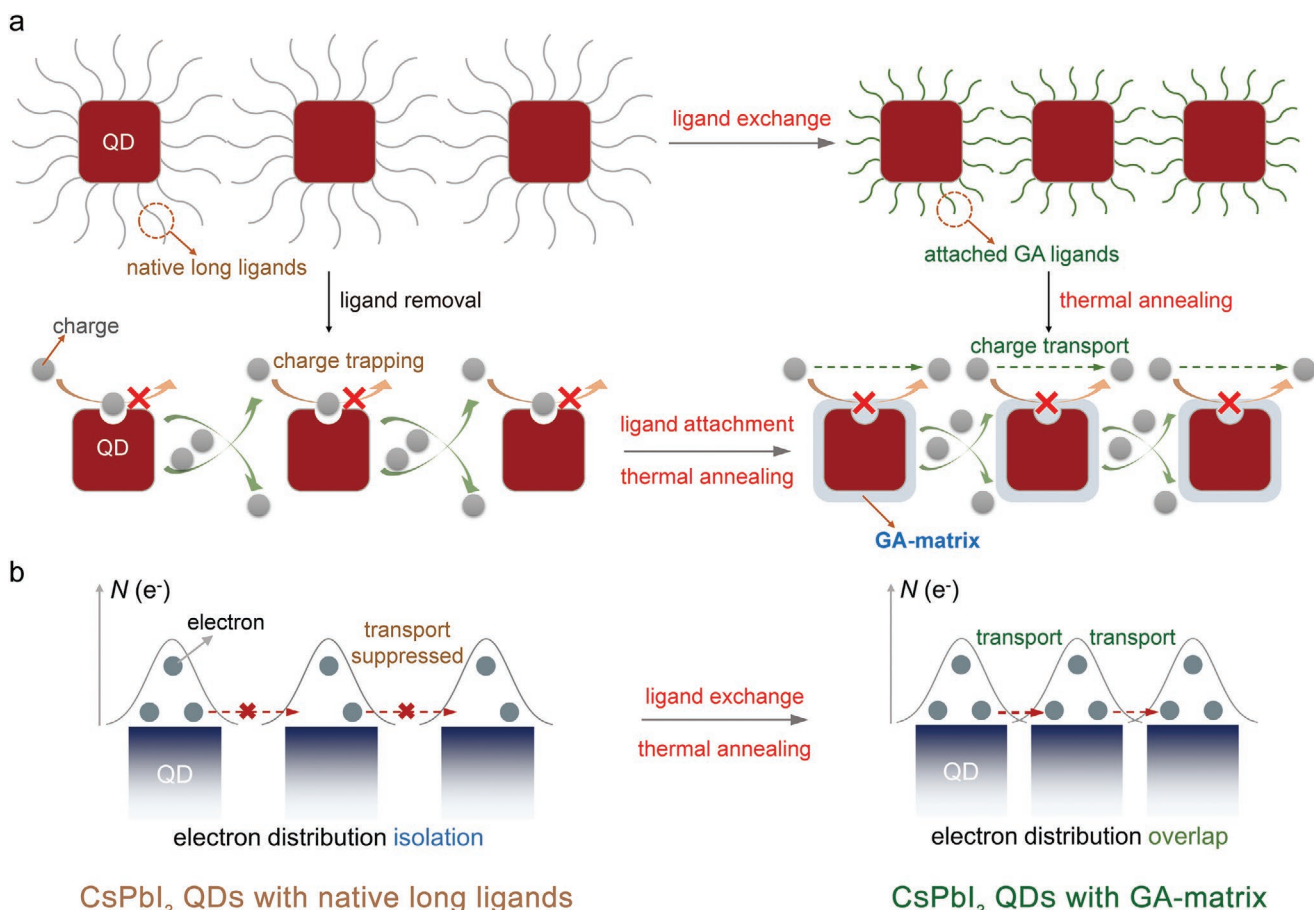


Figure 1. a,b) Schematic diagrams of the formation process of GA-matrix-capped CsPbI_3 QD solids via the ligand exchange process followed by a thermal annealing (“LE-TA” method) induced by GASCN. And its effect on charge transport (a) and enhanced electrical coupling between the GA-matrix-capped CsPbI_3 QD solids as a result of reduced interdot distance (b). It is noted that only one kind of ligands is depicted in each case for better comparison, which does not suggest the QD contains single kind of ligands.

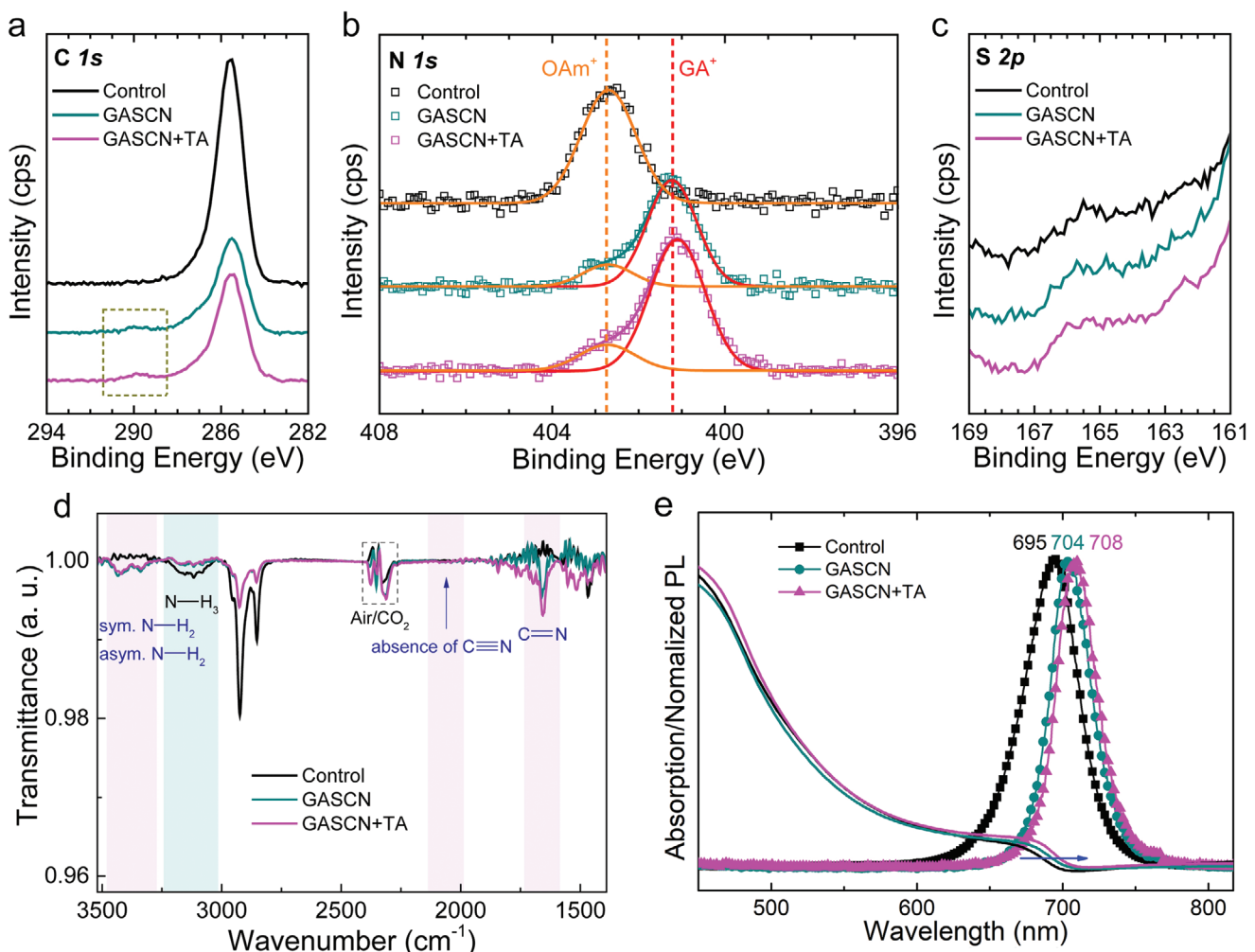


Figure 2. a–c) The XPS core level spectra of CsPbI_3 QD films under different treatments. The background of the peaks in (a) and (b) are subtracted and the raw data of the spectra are shown in (c) for better comparison. d) FTIR and e) UV–vis absorption and steady-state PL spectra of CsPbI_3 QD films under different treatments.

improved charge transport in “LE-TA” CsPbI_3 QD solids indeed delivered a well-performed active layer in the resulting PV devices.

To investigate the surface chemistry of the CsPbI_3 QD solids, we performed X-ray photoelectron spectroscopy (XPS) and Fourier transform infrared (FTIR) spectroscopy measurements on the CsPbI_3 QD films with varying post-treatments (hereafter, the “Control” represents the CsPbI_3 QD film treated only with pure MeOAc, “GASCN” is the one that underwent ligand exchange process induced by GASCN after the MeOAc washing, and “GASCN+TA” is the QD film exchanged by GASCN followed by a mild thermal annealing, that is, “LE-TA” method). The core level spectra of the constituent elements in QDs are shown in Figure 2a–c and Figure S3, Supporting Information, where no significant changes of peak shapes or positions are found among the three samples in the Cs 3d, Pb 4f, and I 3d core level spectra (Figure S3, Supporting Information). Yet the emergence of the peak centered at 290.0 eV in the C 1s core level spectra is indicative of the attachment of GASCN rather than pure EtOAc to the QD surface when the film was treated by

GASCN (Figure 2a and Figure S4, Supporting Information).^[21] Moreover, the N 1s core level spectra in Figure 2b exhibit noticeable variations among the three samples and are fitted to two peaks that attributed to the protonated NH_3^+ group from OAm⁺ (402.7 eV) and the NH_2^+ group in GA⁺ (401.2 eV).^[22,23] When the film was treated with GASCN (0.05 mg mL⁻¹ in EtOAc), the peak intensity at 402.7 eV abruptly decreases while the peak due to the NH_2^+ group in GA⁺ (401.2 eV) appears, which indicates the attachment of shorter GA⁺ to QD surface facilitates the removal of long insulating OAm⁺ ligands. This is consistent with the relative changes in C and N content in the CsPbI_3 QD solids (Table S1, Supporting Information). With respect to SCN⁻ in GASCN (Figure 2c), undetectable differences in the S 2p core level spectra among the three samples suggest the absence of SCN⁻ species in GASCN-treated QD film, indicating that the SCN⁻ presumably would not bond to QD surface during the ligand exchange process. When the GASCN-capped film was further thermally annealed (70 °C), the signals in C 1s and N 1s core level spectra sustain distinctly with slight variation in intensity, likely due to the heat-induced surface arrangement of

QDs (Table S1, Supporting Information). We also found higher concentration (0.5 mg mL^{-1}) of GASCN would result in vanishing of native OAm^+ (at 402.7 eV) but formation of the notorious δ phase in CsPbI_3 (Figure S5, Supporting Information),^[24] the latter of which is detrimental to photoresponse. These findings were also confirmed by the FTIR spectra in Figure 2d. The intensity of resonances due to the oleyl group ($2955, 2922, 2851$, and 1466 cm^{-1}) decreases when the film was treated with GASCN, corroborating the effective removal of long insulating ligands.^[25] The broad resonance centered at 3117 cm^{-1} attributed to stretching vibration of NH_3^+ group in OAm^+ weakens or vanishes when the QD solid film was treated by GASCN. Meanwhile, the concomitant appearance of GA^+ is observed by the emergence of NH_2 symmetric (3337 cm^{-1}), NH_2 asymmetric (3435 cm^{-1}) and $\text{C}=\text{N}$ (1655 cm^{-1}) vibrational modes,^[26,27] confirming the ligand exchange between OAm^+ and GA^+ in CsPbI_3 QD solids when treated with GASCN. Moreover, the absence of $\nu(\text{C}\equiv\text{N})$ resonance near 2060 cm^{-1} in the FTIR spectra after GASCN treatment further confirms that no SCN^- bound to the QD surface during the process (Figure 2d). Both the XPS and FTIR results have demonstrated the formation of GA^+ -coated CsPbI_3 QDs through the “LE-TA” method, which is a prerequisite to the enhancement in electron coupling between adjacent QDs.

We found that the absorption onset shifted to longer wavelength when the film was treated with GASCN as shown in Figure 2e, likely due to the change in the dielectric environment that perturbs the energy of the quantum-confined exciton^[28] or enhanced electron coupling between adjacent QDs compared to the control film.^[8] The optical bandgaps of the films extracted from their Tauc plots were 1.777, 1.767, and 1.761 eV for control,

GASCN and GASCN+TA samples, respectively (Figure S6, Supporting Information). These findings are consistent with the red-shifted photoluminescence (PL) peaks (Figure 2e) in both GASCN-treated samples. Noticeably, the full-width-at-half-maximum (FWHM) of the peaks decreased from 43.63 nm in control to 32.40 and 32.09 nm in GASCN and GASCN+TA films (Figure 2e), respectively, indicating an improved energetic ordering of the QDs.^[29]

The effects of GA^+ capping and thermal annealing on CsPbI_3 QD films morphology and QD solids packing states were investigated by scanning electron microscopy (SEM). As shown in Figure 3a–c, the SEM images clearly resolve the discrete and closely-packed QDs in all samples, indicating the QD structure was retained after the post-treatments. It is worth noting that size of GA^+ (0.556 nm in length)^[30] is much shorter than that of OAm^+ ($\approx 21.573 \text{ nm}$ in length, calculated from the previous report^[31]), indicating the distance between QDs should be dramatically reduced after GA^+ ligand exchange. Here, the particle size of QD solids shows a significant increase after GA^+ -capping (Figure 3b) relative to the control film (Figure 3a), which could be caused by the fusion and coarsening of QDs due to the reduced interdot distance.^[32,12] When it was further annealed, the GA^+ -capped film became more compact with smoother surface morphology due to the heat-induced reassembly of QDs (Figure 3c),^[32] which is also confirmed by the atomic force microscopy (AFM) measurements (Figure S7, Supporting Information). These results suggest the enhanced packing density of CQDs could explain for the enhanced interparticle coupling in the GA -capped CsPbI_3 QD solids. However, heating at the elevated temperature (100°C) would alter the film morphology, generating large cracks or cavities (Figure S8, Supporting

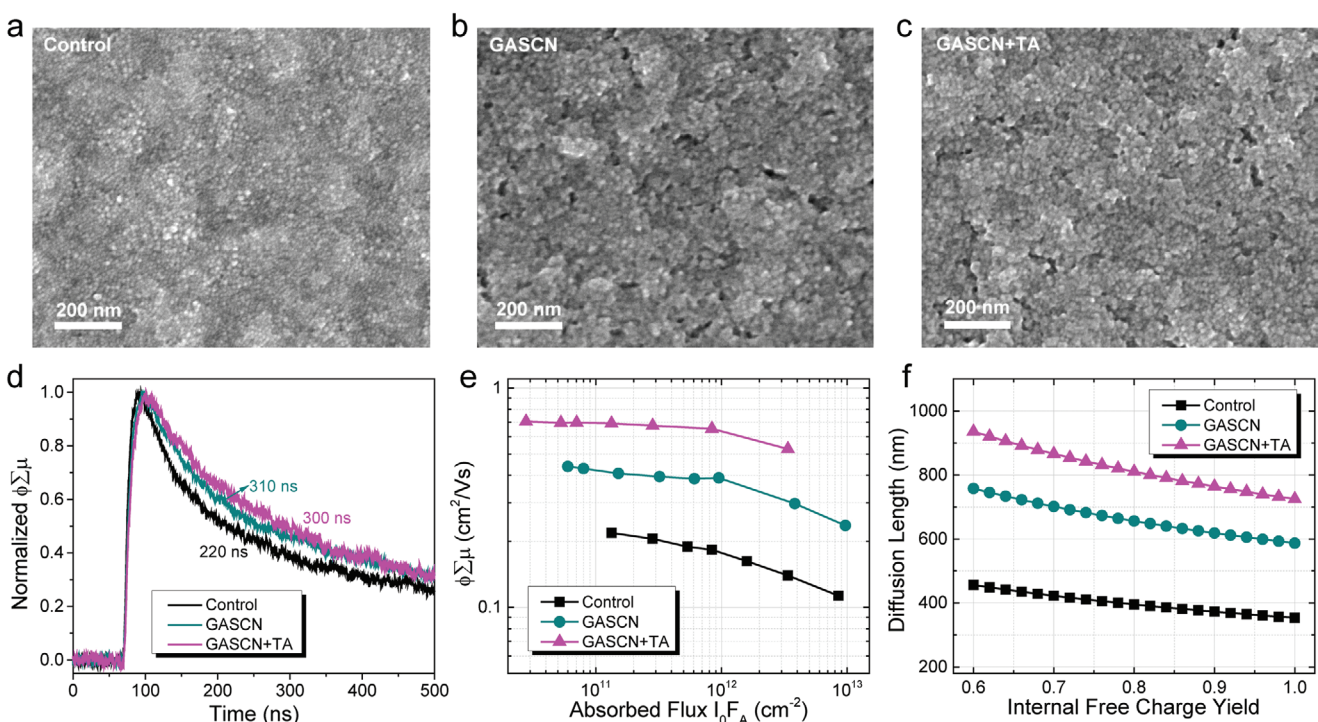


Figure 3. a–c) Top-view SEM images, d) normalized photoconductivity transients (excitation wavelength is 580 nm), e) yield-charge-mobility product ($\phi \Sigma \mu$), and f) free carrier diffusion length of the CsPbI_3 QD films under different treatments.

Information), and induce phase transition to non-perovskite orthorhombic (δ) phase (Figure S9, Supporting Information).^[11] Therefore, it is the combination of GA^+ -capping and mild thermal annealing that strikes a favorable balance between maintaining quantum confinement and forming a compact film.

The charge carrier dynamics in CsPbI_3 QD solids were explored using time-resolved microwave conductivity (TRMC) (Figure 3d–f) measurements.^[17] The photoconductance, ΔG , extracted from the TRMC data, is related to a free-carrier yield-mobility product ($\phi \Sigma \mu$), where ϕ is the quantum efficiency of free charge generation per photon absorbed and $\Sigma \mu$ is the sum of the mobility of electrons and holes in the sample.^[13,17] The TRMC data showed an improvement in the average free carrier lifetime with GASCN-treated films (310 ns for GASCN sample and 300 ns for GASCN+TA sample) compared to the control sample (220 ns) (Figure 3d). The largest improvement was observed in the yield-mobility product ($\phi \Sigma \mu$), where the control ($0.22 \text{ cm}^2 \text{ V}^{-1} \text{ s}^{-1}$) is doubled and tripled for the GASCN ($0.43 \text{ cm}^2 \text{ V}^{-1} \text{ s}^{-1}$) and GASCN+TA ($0.70 \text{ cm}^2 \text{ V}^{-1} \text{ s}^{-1}$) treated films, respectively (Figure 3e), confirming the charge transport within GA-coated CsPbI_3 QD solids is markedly improved as a result of improved electron coupling between QDs. These values correspond to a calculated diffusion length of 353 nm for the control, 587 nm for GASCN, and 725 nm for GASCN+TA-treated films assuming the internal quantum efficiency at the

excitation wavelength (580 nm) is equal to 1.0. These findings suggest that the CsPbI_3 QD solids after GA-assisted “LE-TA” treatment are promising materials in PVs.

To further confirm the “LE-TA” treatment on the QD crystal phase and film crystallinity, grazing-incidence wide-angle X-ray scattering (GIWAXS) is used to probe the crystal features in the pristine and post-treated CsPbI_3 QD film. As shown in Figure 4a–c, all the GIWAXS patterns exhibit typical scattering features of CsPbI_3 QDs.^[10] In specific, the diffraction peaks exhibit no shift in positions in the GA^+ -capped film compared to the control one. When the GA^+ -capped film was further heated at 70 °C, the diffraction positions remain unchanged in Figure 4c, suggesting the crystal structure of CsPbI_3 QD solids maintain intact after heating at this temperature. Besides, as the in-plane line-cuts shown in Figure 4d, all the characteristic diffraction peaks in three samples show no observable changes, well corresponding to the cubic CsPbI_3 crystal structure. All these results confirm the unchanged crystal structure in GA-confined CsPbI_3 QDs after the “LE-TA” process. In addition, the similar crystallinity of bulk QDs after “LE-TA” rules out the possibility that the improved charge transport in CsPbI_3 QD film arises from the improved QD crystallization.

To investigate their PV potential, we fabricated solar cell devices with a structure of glass/fluorine-doped tin oxide (FTO)/ TiO_2 (40 nm)/Pe-QDs (400 nm)/poly(triarylamine) (PTAA, 70 nm)/ MoO_3 (8 nm)/Ag (100 nm) as shown in Figure 5a; the

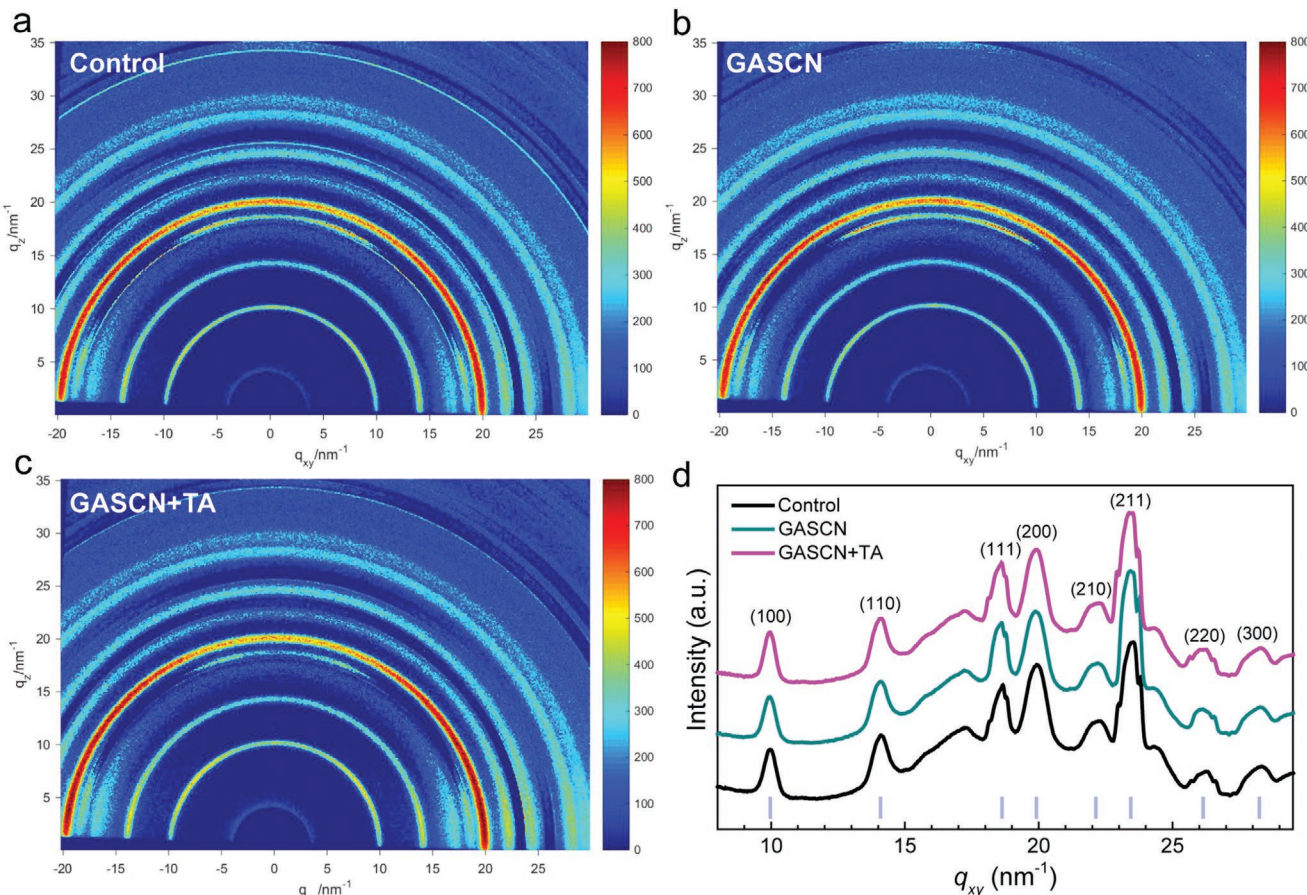


Figure 4. a–c) 2D GIWAXS patterns of CsPbI_3 QD films with different treatments. d) In-plane line-cuts of GIWAXS patterns along the q_{xy} axis.

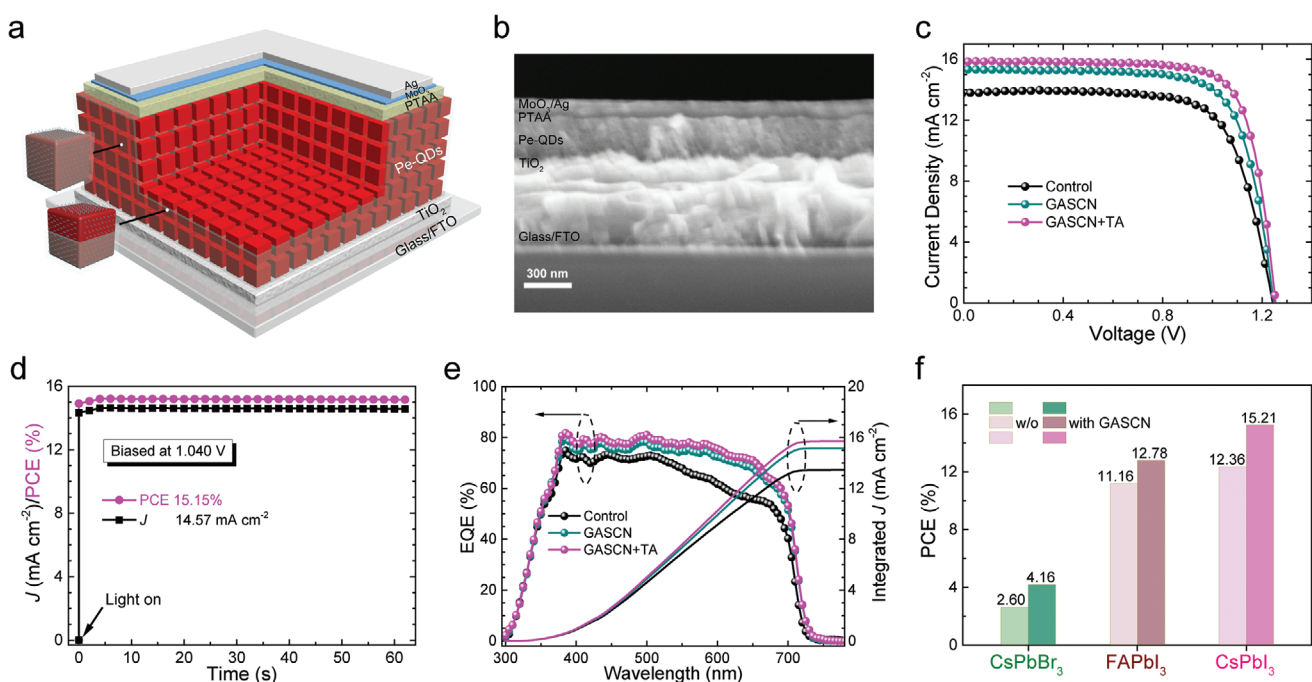


Figure 5. a) Device structure of the CsPbI₃ QDSCs. b) Cross-sectional SEM image of the device. c) J – V curves of the best-performed cells with different treatments to QD films, measured under reverse scan. d) Stabilized current density (J) and PCE of the “champion” CsPbI₃ QDSC. e) EQE curves and integrated J of the best cells. The PV parameters and integrated J values are listed in Table 1. f) The effect of GA-matrix on PCEs of CsPbBr₃, FAPbI₃ and CsPbI₃ QDSCs. The J – V curves and PV parameters of the CsPbBr₃ and FAPbI₃ QDSCs are shown in Figures S19 and S20; Tables S5 and S6, Supporting Information.

detailed device fabrication process is presented in the Experimental Section. Each constituent layer of the device is clearly resolved in the cross-sectional SEM image in Figure 5b. The device optimization includes fine tuning the concentration of the GASCN ligand exchange (LE) solution (Figure S10 and Table S2, Supporting Information) and annealing temperature (Figure S11 and Table S3, Supporting Information). Optimal results were obtained using an LE concentration of 0.075 mg mL⁻¹ and a TA temperature of 85 °C. Figure 5c presents the current density–voltage (J – V) curves of the best-performing CsPbI₃ QDSCs with different treatments measured under the reverse scan under AM 1.5 G, 100 mW cm⁻² simulated solar illumination, with the PV parameters listed in Table 1. The control cell exhibits a PCE of 12.36%, with an open-circuit voltage (V_{oc}) of 1.230 V, J_{sc} of 13.80 mA cm⁻² and a fill factor (FF) of 0.728. When the CsPbI₃ QD film treated by GASCN, the corresponding device shows an increased PCE

of 14.11% with an enhanced J_{sc} up to 15.34 mA cm⁻². Expectedly, the device efficiency further boosts to as high as 15.21% after the QD film was annealed at 85 °C, with a higher V_{oc} of 1.251 V, a J_{sc} of 15.85 mA cm⁻² and an FF of 0.767. In addition, the champion “GASCN+TA” cell shows negligible J – V hysteresis when measured under opposite scan directions (Figure S12, Supporting Information), delivering a stabilized efficiency of 15.15% (Figure 5d). The external quantum efficiencies (EQEs) of the GA⁺-capped devices exhibit obvious improvements between 370 and 700 nm compared to that of the control device, contributing to increased integrated current density (J) values over the AM 1.5G solar spectrum, which are consistent with the improved J_{sc} in GASCN-treated cells from J – V characteristics measurements (Figure 5e). To confirm the reliability of the results, 20 individual cells in several batches were fabricated and the average parameters of these devices were compared, as shown in Figure S13, Supporting

Table 1. PV parameters extracted from J – V curves of CsPbI₃ QDSCs with different treatments to QD films, measured under the reverse scan.

Treatment		V_{oc} [V]	J_{sc} [mA cm ⁻²]	FF	PCE [%]	Integrated J [mA cm ⁻²]
Control	Champion	1.230	13.80	0.728	12.36	13.44
	Average ^{a)}	1.226 (±0.021)	12.97 (±0.61)	0.723 (±0.023)	11.51 (±0.50)	
GASCN	Champion	1.235	15.34	0.745	14.11	15.17
	Average ^{a)}	1.230 (±0.012)	14.67 (±0.37)	0.736 (±0.012)	13.29 (±0.42)	
GASCN+TA	Champion	1.251	15.85	0.767	15.21	15.70
	Average ^{a)}	1.245 (±0.010)	15.61 (±0.28)	0.749 (±0.011)	14.55 (±0.29)	

^{a)}The data were collected from 20 cells and the devices were measured under the reverse scan.

Information and Table 1. The average PCEs of GASCN-treated cells increase from 11.51% for control to 13.29% and further improve to 14.55% after annealing. The narrower PCE distribution in the GASCN+TA-treated devices suggest higher device reproducibility in comparison to the control devices. In addition, the device shelf lifetime was slightly increased by the GA-matrix surface engineering although overall PCEs of CsPbI_3 QDSCs degrade after the storage over 66 h (Figure S14, Supporting Information), which could be improved through the design of mixed-cation Pe-QDs ($\text{Cs}_{1-x}\text{FA}_x\text{PbI}_3$)^[20] or heterojunction structures.^[9,10] It was found that the improvements on PCE were mainly ascribed to the enhanced J_{SC} values, which in turn reflects enhanced charge transport between electrically coupled CsPbI_3 QDs, as the increase in light absorption is insignificant due to the similar thickness of QD layer in both devices (Figure S15, Supporting Information) and negligibly narrowed bandgap of the CsPbI_3 QD after the “LE-TA” process (Figure 2e and Figure S6, Supporting Information). It is also interesting to note that the V_{OC} s of CsPbI_3 QDSCs are significantly higher than that of the state-of-the-art CsPbI_3 polycrystalline film based devices.^[33,15] Although the underlying reasons for this observation are unresolved, they are likely due to quantum confinement effect,^[7] highly crystalline and conformal films, well matched energy levels at the QD/HTL interfaces (Figures S16 and S17, Supporting Information) and/or the absence of either conventional doping or oxidation process of hole transporting layer that damages CsPbI_3 films.^[12,34] Therefore, further studies are warranted to uncover the inherent discrepancies between the QDs- and polycrystalline films-based devices, which could further promote the QDSCs efficiency.

We wondered whether the GA^+ counterion SCN^- , which is not detectably incorporated into the QD films, played any important role in the GA^+ -capping process. As a result, we also investigated another GA-based salt, guanidinium iodide (GAI), on CsPbI_3 QDSCs using the same “LE-TA” procedure (Figure S18, Supporting Information). The GAI-treated device exhibits comparable efficiency with the GASCN-treated one, confirming the crucial role of GA^+ in the formation of matrix-capped CsPbI_3 QD solids, and suggesting a negligible role of the counterion. To evaluate the versatility of our approach beyond just CsPbI_3 compositions, we further applied the GA^+ -assisted “LE-TA” post-treatment to CsPbBr_3 and FAPbI₃ Pe-QDs, with the detailed device performance shown in Figures S19 and S20; Tables S5 and S6, Supporting Information. As summarized in Figure 5f, both CsPbBr_3 and FAPbI₃ QDSCs showed improved PCEs with GA-assisted “LE-TA” post-treatment compared to control devices, suggesting the GA-matrix engineering could be an effective strategy to construct various conductive perovskite QD solids for efficient PVs.

In conclusion, we have demonstrated an efficient method to engineer Pe-QDs surfaces that combines GA^+ ligand exchange and a mild thermal annealing process, which ultimately results in enhanced electrical coupling within and between CsPbI_3 QD solids while maintaining the intact cubic perovskite structure needed for PV performance. The QDSCs based on the conductive CsPbI_3 QD solids delivered a champion PCE of 15.21%. We also demonstrated that the GA^+ -capping matrix formed through the “LE-TA” method also functioned well in other perovskite QDs like CsPbBr_3 and FAPbI₃ QDs, affording a

versatile strategy to regulate the surface of Pe-QDs and boost the efficiencies of Pe-QDSCs.

Experimental Section

Materials: Oleic acid (OA, technical grade 90%), oleylamine (OAm, technical grade 70%), formamidine acetate (99%), and ethyl acetate (EtOAc, anhydrous 99.8%) were purchased from Sigma Aldrich. 1-octadecene (ODE, technical grade 90%), n-hexane (extra-dry 99%), methyl acetate (MeOAc, extra-dry 99%), acetone (analytical reagent, 98%), and guanidinium thiocyanate (GASCN, 99%) were purchased from J&K Scientific Ltd. Lead iodide (PbI_2 , 99%), lead bromide (PbBr_2 , 99.9%), and n-octane (98+) were purchased from Alfa Aesar. Toluene (analytical reagent, 98%) was purchased from Chinasun Specialty Products Co., Ltd. and titanium tetrachloride (TiCl_4 , ≥98%) was purchased from Sinopharm Chemical Reagent Co., Ltd. Guanidinium iodide (GAI, ≥99.5%), formamidinium iodide (FAI, ≥99.5%) and poly(triarylamine) (PTAA, $M_n = 17\,000\text{ g mol}^{-1}$) were purchased from Xi'an Polymer Light Technology Corp., and tris(pentafluorophenyl) borane (95%) was purchased from Acros Organics. All chemicals were used as received without further purification. CsPbI_3 ,^[8] CsPbBr_3 ,^[3] and FAPbI₃^[35] QDs were prepared according to the previous reports.

CsPbI_3 QD Films Fabrication: The GASCN (GAI) solution was prepared by dissolving 16 (12) mg of GASCN (GAI) in 16 (16) mL of anhydrous EtOAc, followed by continuous stirring at 35 °C for 2 h until full dissolution. The GASCN or GAI solutions with various concentrations were obtained by diluting the 1 mg mL^{-1} GASCN or 0.75 mg mL^{-1} GAI solution with EtOAc. The CsPbI_3 QDs in octane (70 mg mL^{-1}) were spin-cast on the TiO_2 substrate at 1000 rpm for 10 s and 2000 rpm for 20 s. Then, 200 μL of MeOAc was loaded onto the QD film for 3–5 s and spun at 2000 rpm for 20 s. This process was repeated for 5 cycles to construct a dense QD film with a thickness of 400–500 nm.^[12,13] Once the desired thickness was achieved, the film was quickly dipped into the neat EtOAc, GASCN or GAI solution for three to five times before rinsed with MeOAc and then immediately dried with N_2 flow. The QD film deposition process was performed in an air-filled glovebox with temperature of 25–28 °C and relative humidity of <10%. The substrates were transferred into a N_2 -filled glovebox and heated at different temperatures for 7 min.

CsPbBr_3 and FAPbI₃ QD Films Fabrication: CsPbBr_3 and FAPbI₃ QD films were prepared using the similar procedure for CsPbI_3 QD film as described above.

QDSCs Device Fabrication: Compact TiO_2 films ($\sim 40\text{ nm}$) were deposited onto the cleaned FTO substrates using chemical bath deposition at 70 °C.^[36] The films were dried at 200 °C for 30 min and then exposed to UV-ozone for 10 min. The CsPbI_3 , CsPbBr_3 , and FAPbI₃ QD films were deposited as described above. PTAA solution (15 mg mL^{-1} in toluene) doped with tris(pentafluorophenyl)borane (dopant/PTAA = 5% in weight) was spin-coated on top of the QD films at 3000 rpm for 40 s.^[34] No extra oxidation or heating process was conducted for the PTAA layer. The QDSCs were completed after subsequent thermal evaporation of 8 nm of MoO_3 and 100 nm of Ag under a vacuum of $<1 \times 10^{-6}\text{ mbar}$. The active area of the devices was 7.25 mm^2 determined by a shadow metal mask.

Measurements and Characterization: The J - V characteristics of the devices were obtained through a Keithley 2400 digital source meter under simulated AM 1.5G spectrum at 100 mW cm^{-2} with a solar simulator (Class AAA, 94023A-U, Newport). Before test, the light intensity was calibrated to 100 mW cm^{-2} by a monocrystalline silicon reference cell (91 150 V, Newport Oriel). The EQE spectra of the cells were recorded through a certified IPCE equipment (Solar Cell Scan 100, Zolix Instruments Co. Ltd.). UV-vis absorption spectra were recorded on a Perkin Elmer model Lambda 750 spectrophotometer. TEM images were captured by the Tecnai G2 F20 S-Twin transmission electron microscope operated at 200 kV. Steady-state PL spectra were obtained through a FluoroMax-4 spectrofluorometer (HORIBA Scientific) with excitation at 465 nm. XPS measurements were performed on a Kratos

AXIS Ultra DLD ultrahigh vacuum photoemission spectroscopy system with an Al $K\alpha$ (1486.6 eV) radiation source. FTIR spectra were recorded on a Bruker HYPERION FTIR spectrometer and cumulated 64 scans at a resolution of 2 cm^{-1} . UPS spectra were obtained using a custom-built ultrahigh vacuum apparatus (base pressure $<4 \times 10^{-10}\text{ mbar}$) equipped with a monochromatized He I radiation (21.22 eV) and a hemispherical electron energy analyzer (Specs PHOIBOS 150). Top-view and cross-sectional SEM images were captured by the Zeiss Supra 55 field emission scanning electron microscope with the extra high tension of 6 kV. GIWAXS measurements were performed in the Shanghai Synchrotron Radiation Facility Laboratory on Beamline BL14B1 using X-rays with a wavelength of 1.24 Å. The TRMC measurements were performed where the sample is placed in a microwave cavity at the end of an X-band waveguide operating at $\approx 9\text{ GHz}$, and is photoexcited through a grid with a 5 ns laser pulse from an OPO pumped by the third harmonic of an Nd:YAG laser.

Supporting Information

Supporting Information is available from the Wiley Online Library or from the author.

Acknowledgements

The authors acknowledge financial support from the National Key Research and Development (R&D) Program of China (Grant No. 2016YFA0202402 and 2017YFA0205002), the National Natural Science Foundation of China (Grant No. 51761145013, 61911530158, 51803144, and 61674111), the Natural Science Foundation of Jiangsu Province of China (BK20170337), and “111” projects. The authors thank the support from Collaborative Innovation Center of Suzhou Nano Science and Technology, Soochow University, the Priority Academic Program Development of Jiangsu Higher Education Institutions (PAPD), and the Soochow University–Western University Center for Synchrotron Radiation Research. The authors also thank Dr. Yingguo Yang at Shanghai Synchrotron Radiation Facility Laboratory for GIWAXS measurements. X.L. acknowledges fellowship support from the China Scholarship Council (CSC) and Postgraduate Research & Practice Innovation Program of Jiangsu Province. This work was authored in part by the National Renewable Energy Laboratory (NREL), operated by Alliance for Sustainable Energy, LLC, for the U.S. Department of Energy (DOE) under Contract No. DE-AC36-08GO28308. The NREL authors acknowledge the Center for Hybrid Organic Inorganic Semiconductors for Energy (CHOISE), an Energy Frontier Research Center funded by the Office of Science, Office of Basic Energy Sciences within the U.S. Department of Energy. The views expressed in the article do not necessarily represent the views of the DOE or the U.S. Government.

Conflict of Interest

The authors declare no conflict of interest.

Keywords

CsPbI₃, guanidinium thiocyanate, ligand exchange, perovskite quantum dots, solar cells

Received: March 19, 2020

Revised: April 23, 2020

Published online: May 25, 2020

- [1] C. R. Kagan, E. Lifshitz, E. H. Sargent, D. V. Talapin, *Science* **2016**, 353, aac5523.
- [2] O. E. Semonin, J. M. Luther, S. Choi, H.-Y. Chen, J. Gao, A. J. Nozik, M. C. Beard, *Science* **2011**, 334, 1530.
- [3] L. Protesescu, S. Yakunin, M. I. Bodnarchuk, F. Krieg, R. Caputo, C. H. Hendon, R. X. Yang, A. Walsh, M. V. Kovalenko, *Nano Lett.* **2015**, 15, 3692.
- [4] L. Protesescu, S. Yakunin, S. Kumar, J. Bär, F. Bertolotti, N. Masciocchi, A. Guagliardi, M. Grotevent, I. Shorubalko, M. I. Bodnarchuk, C.-J. Shih, M. V. Kovalenko, *ACS Nano* **2017**, 11, 3119.
- [5] Q. A. Akkerman, G. Raino, M. V. Kovalenko, L. Manna, *Nat. Mater.* **2018**, 17, 394.
- [6] A. K. Jena, A. Kulkarni, T. Miyasaka, *Chem. Rev.* **2019**, 119, 3036.
- [7] A. Swarnkar, A. R. Marshall, E. M. Sanehira, B. D. Chernomordik, D. T. Moore, J. A. Christians, T. Chakrabarti, J. M. Luther, *Science* **2016**, 354, 92.
- [8] E. M. Sanehira, A. R. Marshall, J. A. Christians, S. P. Harvey, P. N. Ciesielski, L. M. Wheeler, P. Schulz, L. Y. Lin, M. C. Beard, J. M. Luther, *Sci. Adv.* **2017**, 3, eaao4204.
- [9] Q. Zhao, A. Hazarika, X. Chen, S. P. Harvey, B. W. Larson, G. R. Teeter, J. Liu, T. Song, C. Xiao, L. Shaw, M. Zhang, G. Li, M. C. Beard, J. M. Luther, *Nat. Commun.* **2019**, 10, 2842.
- [10] F. Li, S. Zhou, J. Yuan, C. Qin, Y. Yang, J. Shi, X. Ling, Y. Li, W. Ma, *ACS Energy Lett.* **2019**, 4, 2571.
- [11] G. E. Eperon, G. M. Paternò, R. J. Sutton, A. Zampetti, A. A. Haghhighirad, F. Cacialli, H. J. Snaith, *J. Mater. Chem. A* **2015**, 3, 19688.
- [12] J. Yuan, X. Ling, D. Yang, F. Li, S. Zhou, J. Shi, Y. Qian, J. Hu, Y. Sun, Y. Yang, X. Gao, S. Duham, Q. Zhang, W. Ma, *Joule* **2018**, 2, 2450.
- [13] X. Ling, S. Zhou, J. Yuan, J. Shi, Y. Qian, B. W. Larson, Q. Zhao, C. Qin, F. Li, G. Shi, C. Stewart, J. Hu, X. Zhang, J. M. Luther, S. Duham, W. Ma, *Adv. Energy Mater.* **2019**, 9, 1900721.
- [14] K. Chen, W. Jin, Y. Zhang, T. Yang, P. Reiss, Q. Zhong, U. Bach, Q. Li, Y. Wang, H. Zhang, Q. Bao, Y. Liu, *J. Am. Chem. Soc.* **2020**, 142, 3775.
- [15] Y. Wang, M. I. Dar, L. K. Ono, T. Zhang, M. Kan, Y. Li, L. Zhang, X. Wang, Y. Yang, X. Gao, Y. Qi, M. Grätzel, Y. Zhao, *Science* **2019**, 365, 591.
- [16] H. Lee, H.-J. Song, M. Shim, C. Lee, *Energy Environ. Sci.* **2020**, 13, 404.
- [17] M. Suri, A. Hazarika, B. W. Larson, Q. Zhao, M. Vallés-Pelarda, T. D. Siegler, M. K. Abney, A. J. Ferguson, B. A. Korgel, J. M. Luther, *ACS Energy Lett.* **2019**, 4, 1954.
- [18] F. Liu, C. Ding, Y. Zhang, T. Kamisaka, Q. Zhao, J. M. Luther, T. Toyoda, S. Hayase, T. Minemoto, K. Yoshino, B. Zhang, S. Dai, J. Jiang, S. Tao, Q. Shen, *Chem. Mater.* **2019**, 31, 798.
- [19] J. Xi, C. Piao, J. Byeon, J. Yoon, Z. Wu, M. Choi, *Adv. Energy Mater.* **2019**, 9, 1901787.
- [20] M. Hao, Y. Bai, S. Zeiske, L. Ren, J. Liu, Y. Yuan, N. Zarrabi, N. Cheng, M. Ghasemi, P. Chen, M. Lyu, D. He, J.-H. Yun, Y. Du, Y. Wang, S. Ding, A. Armin, P. Meredith, G. Liu, H.-M. Cheng, L. Wang, *Nat. Energy* **2020**, 5, 79.
- [21] J. Tong, Z. Song, D. H. Kim, X. Chen, C. Chen, A. F. Palmstrom, P. F. Ndione, M. O. Reese, S. P. Dunfield, O. G. Reid, J. Liu, F. Zhang, S. P. Harvey, Z. Li, S. T. Christensen, G. Teeter, D. Zhao, M. M. Al-Jassim, M. F. A. M. van Hest, M. C. Beard, S. E. Shaheen, J. J. Berry, Y. Yan, K. Zhu, *Science* **2019**, 364, 475.
- [22] J. Pan, Y. Shang, J. Yin, M. De Bastiani, W. Peng, I. Dursun, L. Sinatra, A. M. El-Zohry, M. N. Hedhili, A.-H. Emwas, O. F. Mohammed, Z. Ning, O. M. Bakr, *J. Am. Chem. Soc.* **2018**, 140, 562.
- [23] A. D. Jodlowski, C. Roldán-Carmona, G. Grancini, M. Salado, M. Lalaiarisoa, S. Ahmad, N. Koch, L. Camacho, G. de Miguel, M. K. Nazeeruddin, *Nat. Energy* **2017**, 2, 972.

- [24] S. Kajal, G.-H. Kim, C. W. Myung, Y. S. Shin, J. Kim, J. Jeong, A. Jana, J. Y. Kim, K. S. Kim, *J. Mater. Chem. A* **2019**, *7*, 21740.
- [25] L. M. Wheeler, E. M. Sanehira, A. R. Marshall, P. Schulz, M. Suri, N. C. Anderson, J. A. Christians, D. Nordlund, D. Sokaras, T. Kroll, S. Harvey, J. J. Berry, L. Y. Lin, J. M. Luther, *J. Am. Chem. Soc.* **2018**, *140*, 10504.
- [26] M. Li, L. Yang, S. Fang, S. Dong, S.-i. Hirano, K. Tachibana, *Polym. Int.* **2012**, *61*, 259.
- [27] L. Dimesso, A. Quintilla, Y. M. Kim, U. Lemmer, W. Jaegermann, *Mater. Sci. Eng. B* **2016**, *204*, 27.
- [28] C. A. Leatherdale, M. G. Bawendi, *Phys. Rev. B* **2001**, *63*, 165315.
- [29] J. Xu, O. Voznyy, M. Liu, A. R. Kirmani, G. Walters, R. Munir, M. Abdelsamie, A. H. Proppe, A. Sarkar, F. P. Garcia de Arquer, M. Wei, B. Sun, M. Liu, O. Ouellette, R. Quintero-Bermudez, J. Li, J. Fan, L. Quan, P. Todorovic, H. Tan, S. Hoogland, S. O. Kelley, M. Stefik, A. Amassian, E. H. Sargent, *Nat. Nanotechnol.* **2018**, *13*, 456.
- [30] N. D. Marco, H. Zhou, Q. Chen, P. Sun, Z. Liu, L. Meng, E.-P. Yao, Y. Liu, A. Schiffer, Y. Yang, *Nano Lett.* **2016**, *16*, 1009.
- [31] S. Mourdikoudis, L. M. Liz-Marzán, *Chem. Mater.* **2013**, *25*, 1465.
- [32] S. J. Baik, K. Kim, K. S. Lim, S. Jung, Y.-C. Park, D. G. Han, S. Lim, S. Yoo, S. Jeong, *J. Phys. Chem. C* **2011**, *115*, 607.
- [33] P. Wang, X. Zhang, Y. Zhou, Q. Jiang, Q. Ye, Z. Chu, X. Li, X. Yang, Z. Yin, J. You, *Nat. Commun.* **2018**, *9*, 2225.
- [34] J. Luo, J. Xia, H. Yang, L. Chen, Z. Wan, F. Han, H. A. Malik, X. Zhu, C. Jia, *Energy Environ. Sci.* **2018**, *11*, 2035.
- [35] A. Hazarika, Q. Zhao, E. A. Gaulding, J. A. Christians, B. Dou, A. R. Marshall, T. Moot, J. J. Berry, J. C. Johnson, J. M. Luther, *ACS Nano* **2018**, *12*, 10327.
- [36] A. Yella, L. P. Heiniger, P. Gao, M. K. Nazeeruddin, M. Gratzel, *Nano Lett.* **2014**, *14*, 2591.